Design and Validation of a Synchronous Reluctance Motor with Single Tooth Coils

Christopher. M. Spargo, *Member, IEEE*, Barrie. C. Mecrow, *Member, IEEE*, James. D. Widmer and Christopher Morton and Nick Baker

***Abstract*—This paper presents for the first time the analysis and experimental validation of a 6-slot 4-pole synchronous reluctance motor with non-overlapping fractional slot-concentrated windings. The machine exhibits high torque density and efficiency due to its high fill factor coils with very short end windings, facilitated by a segmented stator and bobbin winding of the coils. These advantages are coupled with its inherent robustness and low cost. The topology is presented as a logical step forward in advancing synchronous reluctance machines which have been universally wound with a sinusoidally distributed winding. The paper presents the motor design, performance evaluation through finite element studies and validation of the electromagnetic model and thermal specification through empirical testing. It is shown that high performance synchronous reluctance motors can be constructed with single tooth wound coils but considerations must be given regarding torque quality and the d-q axis inductances.**

***Index Terms*—AC motor drives, concentrated winding, finite element method, reluctance, synchronous machine.**

I. Introduction

SYNCHRONOUS reluctance machines conventionally utilize polyphase distributed windings [1-6], which have long end windings, the consequence of which is a large redundant copper mass and corresponding copper loss in an end region that is usually difficult to cool [7]. These windings also typically have a low slot fill factor, between 0.3 and 0.4 [8], leading to low torque density, high copper loss and laborious manufacture of stator coils. The authors have previously proposed the use of fractional slot concentrated windings (FSCW) in synchronous reluctance machines as a logical step to realizing a higher torque density and efficiency machine [9-11]. Application of fractional slot concentrated windings reduces the end winding length, reducing both machine mass and copper loss, a benefit of which the switched reluctance motor inherently enjoys [12] and have also been investigated for induction motors [13]. There are many advantages to designing a synchronous reluctance machine with fractional slot concentrated windings [9] which increase with pole number [10]. Increased torque density and machine efficiency can be achieved over that of a conventional sinusoidally distributed machine, with improved thermal properties, easier and lower cost when manufacturing with simple robust designs. This is mainly due to the short end windings and attainable high slot fill factors, assisted by stator segmentation [14,15]. However, low power factors and high torque ripple were reported due to a high level of space harmonic content in the machine MMF profile. The topology presented is similar to that of a switched reluctance motor, but is however a true rotating field AC machine that is fed by a conventional polyphase voltage source inverter, unlike the switched reluctance machine (SRM) which requires a non-standard converter and generally high torque ripple [12] for equal phase number, also requiring extra current sensors and phase connections. Fig. 1 shows a 3D model of the designed fractional slot concentrated winding synchronous reluctance machine (cSynRM).

The authors are with the School of Electrical and Electronic Engineering, Newcastle University, Newcastle upon Tyne, NE1 7RU, UK. (e-mail: c.m.spargo@ncl.ac.uk).

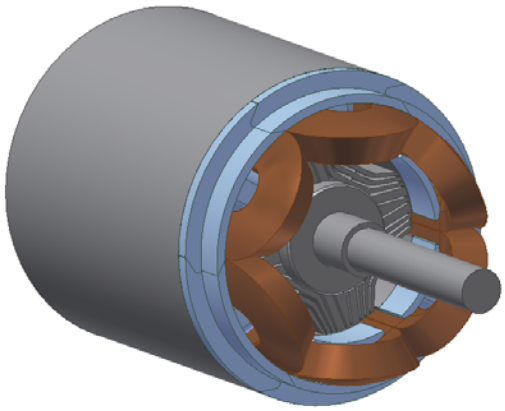

Fig. 1. 3D model of the designed 6-slot 4-pole synchronous reluctance motor with non-overlapping fractional-slot concentrated windings.

This paper presents the first design, analysis, prototyping and verification of a single tooth wound synchronous reluctance motor. Through finite element and empirical validation, the machine is shown to exhibit heightened torque density and efficiency, though suffers from a low power factor. Sections III and IV outline motor stator/winding and rotor design respectively. Section V details finite element performance predictions and includes findings relating to the *d-q* axis inductances and torque quality in the cSynRM. Section VI presents the prototype machine and experimental rig and Section VII presents the experimental validation of the electromagnetic model and analytical comparison.

II. Specification

The machine is designed according to the frame size, with a casing inside diameter of 150mm and accommodation for a motor of length 200mm. The machine has no special cooling provisions and is of the totally enclosed non-ventilated

(TENV) type. The outer machine dimensions were chosen to be comparable to other machines designed in-house for research purposes. The machine specification is presented in Table I.

TABLE I
MACHINE SPECIFICATION

Parameter	Value
Stator outer diameter [mm]	150
Active stack length [mm]	150
Shaft diameter [mm]	20
Base speed [rpm]	1500
Number of phases	3
DC link voltage [V]	590
Cooling	TENV
Winding Type	FSCW Star Connected

III. STATOR AND WINDING DESIGN

The machine is a three phase motor, m=3, and is designed with a fractional slot-concentrated winding, which utilizes coils with a span of one tooth and are hence non-overlapping. Applicable slot-pole combinations that support fractional slot concentrated windings are limited with low pole numbers, as represented in Table II [16].

TABLE II
APPLICABLE SLOT-POLE COMBINATIONS (WINDING FACTORS)

Number of Slots (Q_s)	Number of Pole-Pairs (p)		
	1	***2***	***3***
3	0.866	0.866	-
6	0.866	**0.866**	-
9	0.617	0.617	0.866

In order to maximize the fundamental winding factor k_{w1} and minimize the space harmonic content, a double layer winding is chosen ($n_l = 2$). For a four pole machine, $p = 2$ with a slot number $Q_s = 6$ which supports a fractional slot concentrated winding, the number of slots per pole per phase [17];

$$q = \frac{Q_s}{2mp} = \frac{z}{n} = \frac{1}{2} < 1 \quad (1)$$

Thus, due to the even denominator of Eq. (1), the winding is classified as a Grade I winding with applicable harmonic ordinates [17];

$$v = \pm\left(\frac{1}{n}\right)(6g + 2); \text{where } g \ \pm 1,2,3,4 \ldots \quad (2)$$

The harmonics therefore take on the values, 1, -2, 4, -5, 7… etc. The significance of the negative is that these space harmonics are counter-rotating space harmonics with respect to the fundamental. Odd and even harmonics exist due to air gap flux asymmetry over two rotor pole pitches. The winding factors can then be analytically determined;

$$k_{wv} = \sin\left(\frac{\pi p}{Q_s}\right)\frac{\sin\left(\frac{v\pi}{2m}\right)}{nq\sin\left(\frac{v\pi}{2mnq}\right)} \quad (3)$$

Thus by substitution $k_w = \frac{\sqrt{3}}{2} = 0.866 = \text{constant}.$ The winding factors for all harmonics are equal to that of the fundamental torque producing winding factor, leading to significant space harmonic content. The winding factors of the selected winding and the respective MMF harmonics are presented in Figure. 2. The winding layout is presented in Figure. 3 and the airgap periphery MMF distribution is presented in Figure. 4.

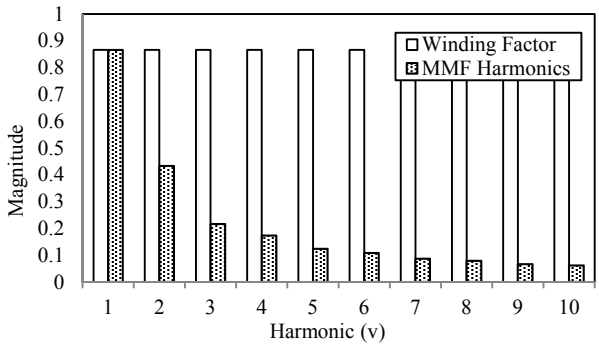

Fig.2. Winding factors and MMF spatial harmonics of a 6-slot 4-pole double layer fractional slot concentrated winding.

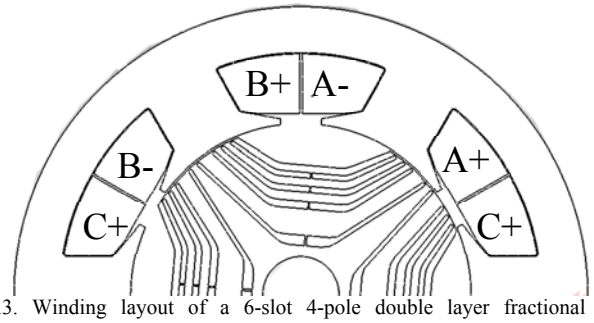

Fig.3. Winding layout of a 6-slot 4-pole double layer fractional slot concentrated winding.

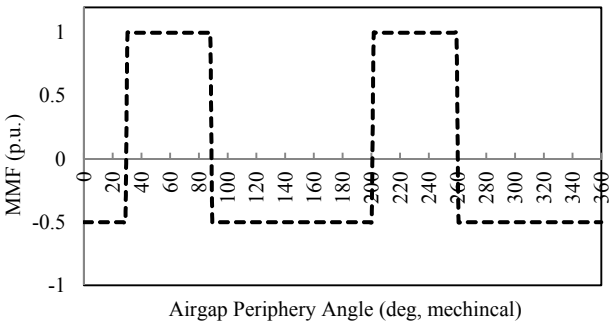

Fig. 4. Three phase MMF distribution of the 6-slot 4-pole fractional slot concentrated winding synchronous reluctance machine; I_a=1A, I_b=I_c=-0.5A

An important consideration in a machine of this type is the end winding length, as the short end windings of the single tooth coils facilitate the machines superior performance over a conventional synchronous reluctance motor, the end length can be approximated [18];

$$l_{\text{end}} = 0.93\left(\frac{\pi r_w}{Q_s}\right) \quad (4)$$

Where twice the average coil radius $4r_w \cong D_{sso} - D_{ssi}$ (difference between the stator outer and inner diameters) relates to the coil axial extent approximately as $l_{\text{axial}} \cong \frac{l_{\text{end}}}{\pi}$,

assuming a semi-circular end winding. The end winding turn length is approximated to be 53mm, the phase resistance is determined as 222mΩ and end turn resistance of 56mΩ with an axial extent of 19mm, assuming a fill factor of 60% and 52 turns per coil, which is achievable practically. The approximate slot area is 560 mm^2. A wire diameter of 2mm is used with Grade II Class F insulation.

The main dimensions of the stator segment of the designed machine is presented in Fig. 5.

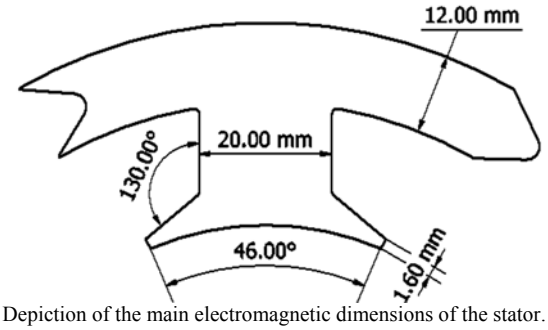

Fig.5. Depiction of the main electromagnetic dimensions of the stator.

The stator is segmented (as in Figs. 5 & 6) to aid coil winding and ease of construction. The tooth can be wound before assembly resulting in high fill factors. In this machine, a slot fill factor (including insulation) of 59% is achieved. A shrink fit of the assembled stator into the case ensures that any small inter-segment air gaps are closed up tightly as to not significantly affect the magnetizing inductance and machine performance.

Fig.6. Stator end windings showing segments assembled in the case.

IV. Rotor Design

The rotor design is very important in this machine as the high space harmonic content causes unwanted parasitic effects [9-11]. Well known design rules [19,20] were obeyed, such as thin radial and tangential ribs, an optimized number of barriers (4+cutout) and a *q*-axis insulation ratio of approximately 0.5. The optimised rotor design (Fig. 7) is presented briefly here (with both modelled and measured parameters summarised in Table III) but is considered in detail by the authors through a novel finite element post processing technique [11].

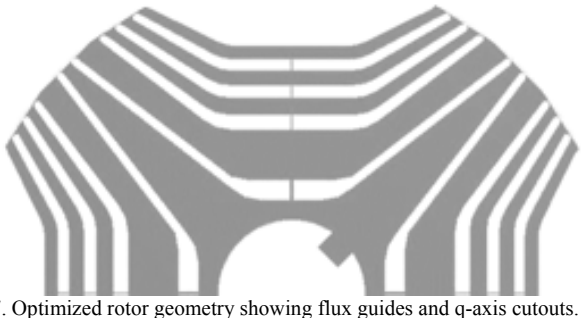

Fig.7. Optimized rotor geometry showing flux guides and q-axis cutouts.

TABLE III
Rotor Parameters

Parameter	Value/FEA	Measured
Rotor outer diameter [mm]	89	-
Active stack length [mm]	150	-
Number of barriers	4 + cutout	-
Number of layers	9	-
Insulation ratio (q-axis)	0.5	-
Saliency Ratio (Unsaturated)	3.70	~4.4
Unsaturated d-axis inductance (mH)	38.51	41.56
Unsaturated q-axis inductance (mH)	9	9.44

As the airgap fields contain harmonics, derived from the high MMF space harmonic content, a large torque ripple is a consequence. In this machine topology and slot pole combination, it is found [11] that the second order field harmonic (8-pole counter-rotating) is the offending harmonic field. Thus reduction of the interaction of this harmonic with the rotor is of the utmost importance – this can be realised by reducing the effective rotor saliency for the 8-pole field. As described in [11] simple rotor cutouts with a span based on the offending harmonic wavelength can reduce this saliency and improve the torque quality in the machine. Section IV will investigate this torque quality issue further. Mechanical finite element analysis (ANSYS Mechanical) predicts that the rotor component is safe to 10,000 rpm with a safety factor of 2 using M270-35A lamination material. The radial and tangential rib thicknesses are 0.5mm and 0.3mm respectively, these thicknesses minimize the *q*-axis flux for high performance but limit the safe maximum rotor speed. Stress is shown at 5,000 rpm in Figure. 8 with peak stress in the radial ribs of 90MPa.

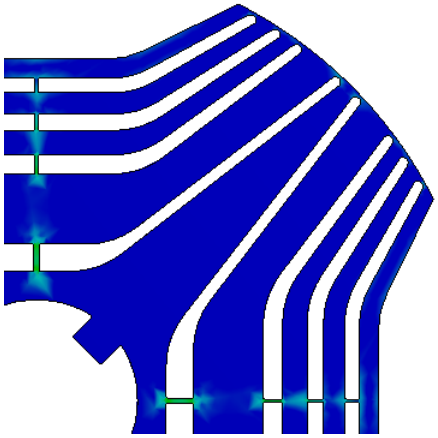

Fig.8. Rotor stresses confined to the radial ribs.

V. Finite Element Analysis

Finite element analysis (FEA) is used to verify the design and calculate the machine's performance. It is also used to investigate the *d-q* axis inductance and the torque quality of the machine. The FEA tool used is Infolytica MagNet coupled with Infolytica Motorsolve. The finite element analysis is then later verified by experimental testing of a prototype machine.

A. Rated Performance

The rated operating point is based on a total machine loss of approximately 340W (copper + iron) at a synchronous speed of 1500rpm (50Hz), through simulation the rated line current is determined to be 21.2A RMS. Figure 9 shows the FEA computed fields and finite element mesh under maximum torque control at rated speed and line current (no time harmonics). Figure 10 shows the torque and voltage waveforms at this operating point.

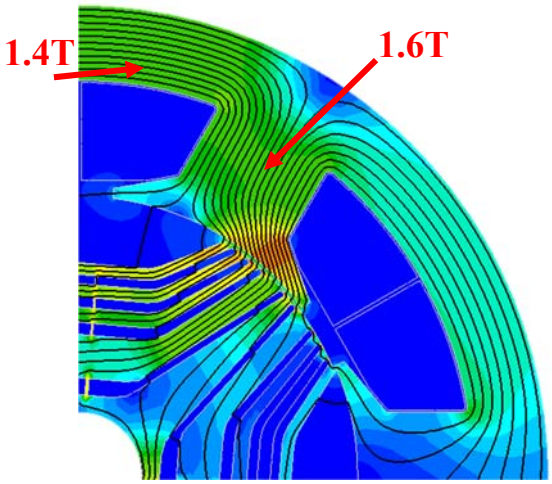

Fig. 9. Finite element flux plot showing field lines and saturation levels at rated operating point.

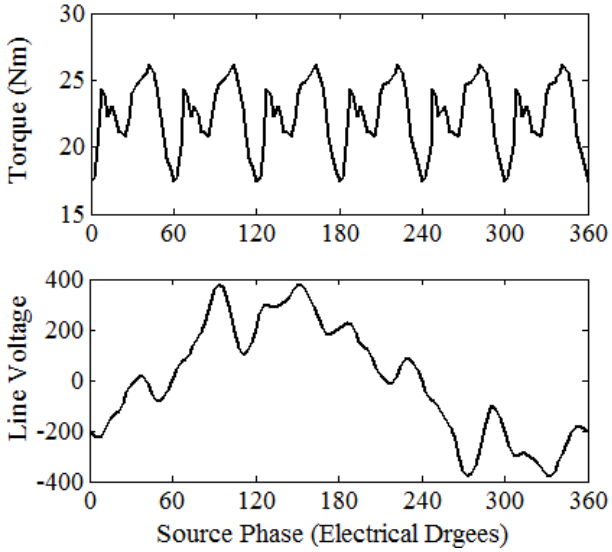

Fig.10. Above – FEA torque waveform at rated operating point. Below – FEA voltage over one electrical cycle.

The torque at rated current (current density of 6.75A.mm^{-2}) and speed is 21.8Nm, equating to a power of 3.5kW and a torque (power) density of 1.02kNm.m^{-3} (160kW.m^{-3}). The RMS phase voltage is 230V, corresponding to the end of the constant torque region (base speed). Figure 11 shows the torque capability (based on transient analysis) of the machine with respect to stator current density, showing a large overload capability and that the MTPA trajectory follows current angle 45 degrees very closely.

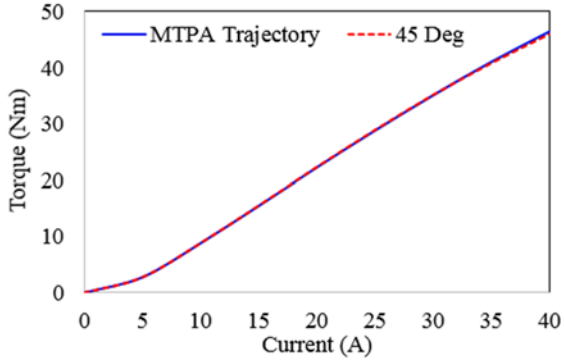

Fig. 11. Mean torque vs current density showing a good overload capability.

At the rated operating point a total loss of 348W is calculated through finite element analysis. Table. IV presents the loss distribution at rated operating point. The hysteresis loss dominates the iron losses (17% of total losses), concentrated in the stator coreback and teeth. The stator copper loss is 308W, which equates to a machine energy conversion efficiency of approximately 91%.

TABLE IV
Iron Losses

Loss	Stator Coreback	Stator Teeth	Rotor Core	Stator Winding
Copper	-	-	-	308
Eddy	1.44	1.41	2.5	-
Hysteresis	12.4	11.3	8.4	-

The machine exhibits a power factor of 0.48, which is reduced due to the increased harmonic leakage flux in the machine. Thus, the machine exhibits a high torque density and high efficiency but has a low power factor, when compared to conventional synchronous reluctance machines, as suggested in [9].

B. d-q Axis Inductances

The *d-q* transformation is usually derived with integral slot windings in mind, assuming no space harmonic content in the airgap. This transformation effectively reduces the spatially varying inductances to constants (neglecting saturation) attributed to the *d-q* axes [21]. With fractional slot concentrated windings, high levels of space harmonics exist in the airgap and therefore a fundamental assumption of *d-q* axis theory does, strictly, no longer apply. In machines with $q > 1$ the inductances L_d and L_q are constant and do not exhibit any spatial or temporal variation in linear or saturated machine operation. However, in machines with $q < 1$, as presented in Figs. 12 and 13, the inductances L_d and L_q vary with rotor angle, thus, it can be concluded that this affects machine performance, applicability of sensorless control [22] and accuracy of dynamic simulations. Figures. 12 and 13 show the spacial variation of the axis inductances, calculated by finite element studies of the designed machine. In this case, the *d*- and *q*-axes are selected by rotating the rotor with respect to the

magnetic axis of Phase A, with phases energized as $i_a = 1\,\text{p.u.}, i_b = i_c = -0.5\,\text{p.u.}$

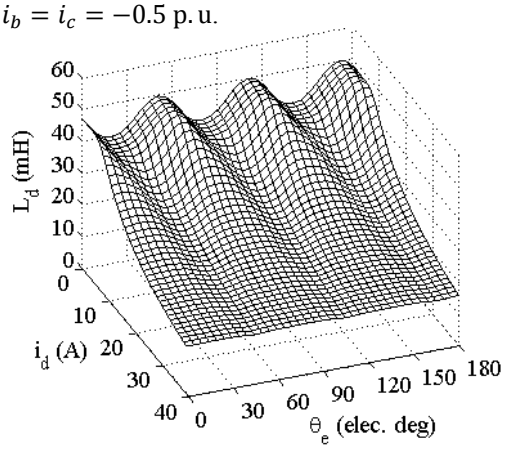

Fig. 12. *d*-axis inductance as a function of rotor position and d-axis current over one electrical cycle.

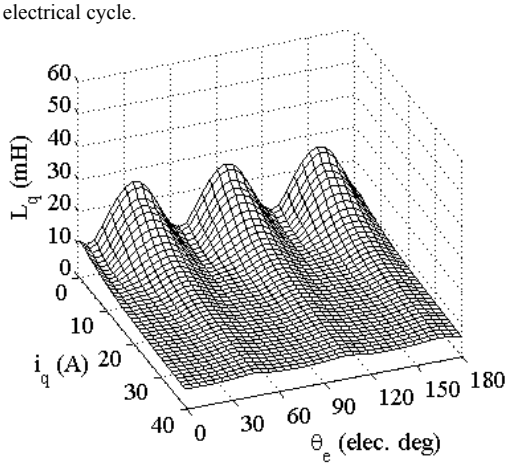

Fig. 13. *q*-axis inductance as a function of rotor position and q-axis current over one electrical cycle.

At rated current the variation of the inductances are almost sinusoidal – the variation $\Delta L_d = 5\text{mH}$ and $\Delta L_q = 8\text{mH}$, the harmonic order of this variation with respect to the machine fundamental frequency is $v = 6$, as presented in Fig. 14.

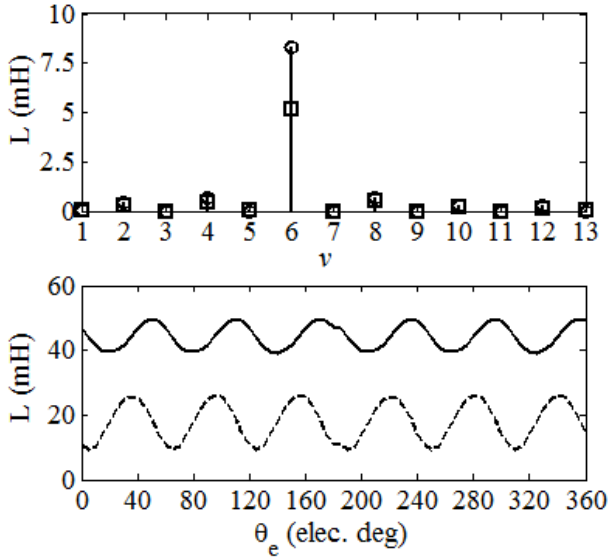

Fig. 14. Upper: Harmonic decomposition. Lower: Inductance waveforms. Inductances correspond to Figs, 11 and 12.

This 6th harmonic inductance, corresponds to the 2nd order airgap field harmonic, $v = 2(v_1 - v_n)$, where v_n is calculated from Eq. 2. With the 8 pole counter rotating field $v_n = -2$, the inductance harmonic is calculated as $v = 6$.

Therefore in the cSynRM, spacial variation of the *d-q* inductances is significant. This 6th harmonic derives from the non-sinusoidal distribution of coils. The influence of increased axis current reduces the inductance variation due to dominance of magnetic saturation in the main magnetic circuit. This variation needs to be considered in drive control schemes, especially in sensorless control schemes, requiring multidimensional lookup tables stored. These findings are similar to those previously reported where the influence of sub-harmonics in certain machine geometries was observed to cause temporal and spacial variation of the *d-q*-axis inductances in an IPM (interior permanent magnet) motor [23], where it has also been noted the inadequacy of *d-q* theory [24]. In the case of the synchronous reluctance motor, as the airgap length is small due to its inverse relation with the machine magnetizing inductance, power factor and torque capability, the localized effects caused by the higher order harmonics are increasingly pronounced on the *d-q* axis inductances

C. Torque Quality

The torque ripple shown in Fig. 11 is 44% of the average torque, which is still high. This ripple is however greatly reduced by the authors [11] from an unoptimised rotor configuration where the torque ripple exceeds 100%. As the rotor has parasitic saliencies that link with their respective airgap harmonics, torque ripple occurs as a result, detailed in Section III. The tangential stress on the rotor;

$$\sigma_{\tan}(\theta,t) = \sum_{v=1}^{\infty} H_{\theta v}(\theta,t) B_{rv}(\theta,t) \tag{5}$$

Can be used for calculation of the resultant rotor electromagnetic torque at a time instant by integrating over the surface (adapted from [11]);

$$T_\theta(t) = r^2 \int_0^{l_a} \int_0^{2\pi} \sum_{v=1}^{\infty} H_{\theta v}(\theta,t) B_{rv}(\theta,t)\; d\theta dz \tag{6}$$

Thus the harmonic fields due to the parasitic asynchronous MMF spatial harmonics directly contribute to the torque ripple in the machine, degrading the torque quality. The prototype rotor design minimizes this through improved electromagnetic design.

V. Prototype Construction and Test Rig

The prototype machine laminations (M250-35A) were electro-discharge machined in a glued stack. The completed rotor component is presented in Figure 15.

Fig. 15. Prototype rotor lamination stack on the motor shaft before insertion of the stator.

The stator segments depicted in Fig. 5 are cut separately, bobbin wound with 2mm Grade II Thermal Class F magnet wire, 52 turns, using 0.3mm slot liner. End caps were milled from high temperature plastic to act as end winding guides so that neat coils could be wound and to minimise the chance of coil to iron segment short circuits on the lamination edges. The achieved coil fill factor is 60.63%, where the slot fill factor is 58.6%, a summary of the predicted and measured phase resistances and end winding length is presented in Table. V.

TABLE V
WINDING MEASUREMENTS

Parameter	Predicted	Measured
Phase Resistance [Ω]	0.23	0.23
End winding axial extent [mm]	19	18.6

The stator was assembled in a jig and shrunk into the aluminum case, this closes up any airgaps between segments. The rotor-stator airgap was measured with feeler gauges to be 0.5mm. Figure. 16 shows the completed prototype (including rotor) with the main dimensions indicated.

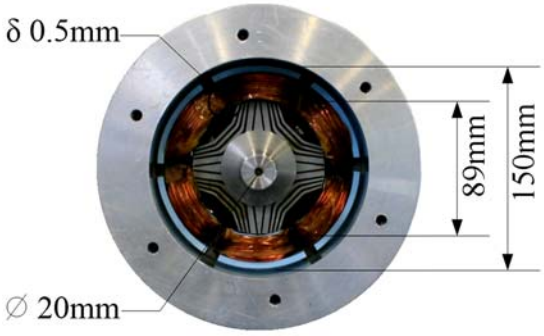

Fig.16. End view and main dimensions of the prototype motor.

The test setup to experimentally verify the magnetic circuit consists of the prototype motor coupled through a torque transducer to a machinists dividing head. A programmable 16kW DC power supply was used as excitation. Figure. 17 shows the test setup.

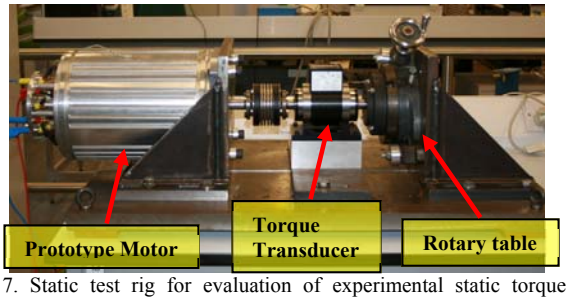

Fig. 17. Static test rig for evaluation of experimental static torque and magnetization curves.

VI. EMPIRICAL VALIDATION

Static testing of the magnetic circuit was performed in order to validate the torque producing capability, *d-q* axis flux linkages and inductances. Measurements are compared with 2D FEA which is compensated for end effects using lumped end winding leakage inductance of 139.5 μH, determined analytically and confirmed through finite element calculations (see Appendix).

A. Torque Capability

Figure 18 shows the static torque results, both finite element (solid) and experimental (dashed), an excellent match between the calculated and measured results is observed confirming the torque density of the motor.

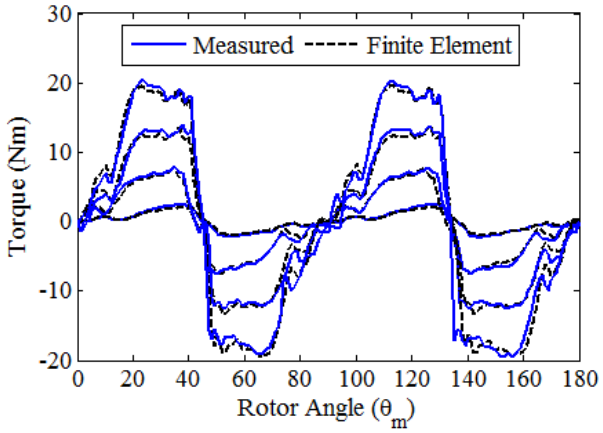

Fig. 18. Experimental and finite element static torque curves over 180 electrical degrees for 5A, 10A, 15A and 20A equivalent DC current.

B. Flux Linkage Functions

The direct and quadrature axis flux linkage was obtained using the *direct flux linkage technique*, based on numerical computation of the following equation [12];

$$\psi_{d,q}[t] = \int_0^t v_{d,q}[t] - R_s i_{d,q}[t] dt \qquad (7)$$

Figs. 19 and 20 show the applied voltage and current waveforms and the comparison of finite element and experimental magnetization curves.

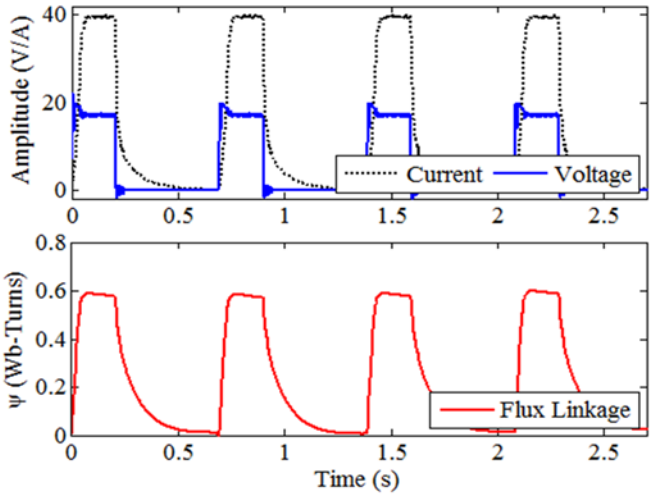

Fig. 19. Measured voltage, current and flux linkage waveforms.

The applied current I_{DC} is translated into phase currents $I_A = 1\text{p.u.}$; $I_B = I_C = -0.5\text{p.u.}$ Experimental direct axis magnetization data matches very closely with the predicted direct axis flux linkage. The quadrature axis FEA prediction is also followed closely by the experimental data, however error at higher currents is increased due to the inadequacy of the lumped element stator end winding leakage inductance in the model.

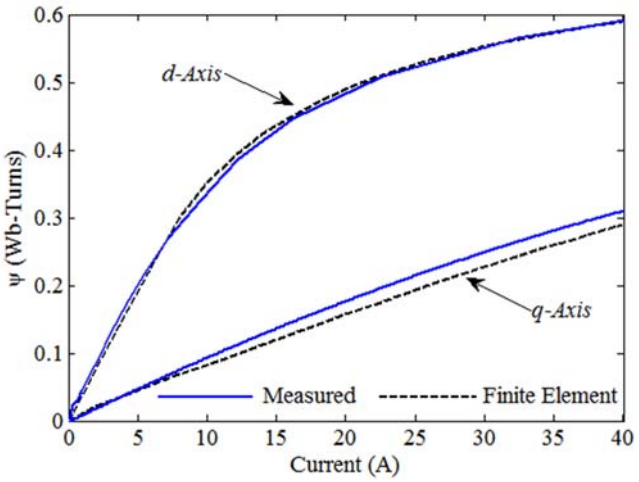

Fig. 20. Experimental and finite element *dq*-axis magnetisation curves.

The presented experimental magnetization curves therefore validate the magnetic circuit design and also the finite element model used for performance prediction of the cSynRM topology.

C. Inductances

Figure 21 shows the FE and experimentally determined d-q axis inductances, calculated form the flux linkages in the respective axes, which are again in very close agreement.

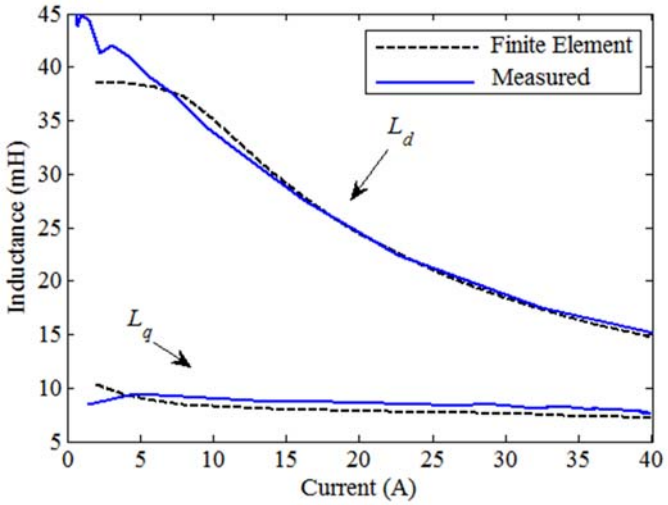

Fig. 21. Experimental and finite element *dq*-axis inductances.

D. d-q Theory

At a rated current of 21.2A, L_d=23.48mH and is L_q=8.33mH, therefore the motors true saliency ratio ξ at the rated current is approximately 2.98 and the torque index $\Theta = |L_d - L_q|$ is approximately 15.5. Using conventional *d-q* theory [21], the power factor and mean torque can be calculated under maximum torque per ampere control;

$$\cos(\varphi) = \frac{\xi - 1}{\sqrt{2}} \sqrt{\frac{1}{\xi^2 + 1}} \tag{8}$$

$$t_{em} = \frac{3}{2} p \Theta i_s^2 \tag{9}$$

Thus, the calculated power factor is 0.45 and a mean electromagnetic torque of 21Nm, which corresponds closely to the 21.8Nm finite element prediction, showing that *d-q*-analysis in this case provides accurate predictions of mean torque and power factor in a machine with fractional slot-concentrated windings, the power factor is lower as the theory does not include space harmonics. Though mean values are accurate, during steady state, the conventional model is not guaranteed to accurately predict transient or instantaneous behavior of the machine.

E. Thermal Measurements

Current controlled DC was provided to series connected stator coils to provide 300W of continuous copper loss, representative of the winding loss at rated load. Thermocouples located on the case, end winding, slot and coreback measured the temperature rise over an 8 hour period. Fig. 22 shows the temperature measurements over this period.

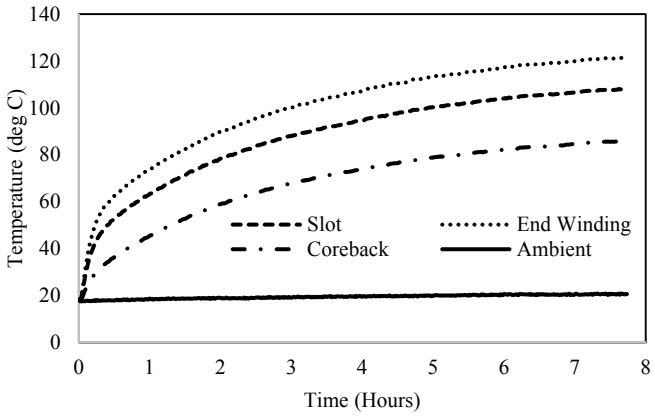

Fig. 22. Experimental temperature rise under rated loss conditions.

The temperature hotspot is in the end winding (122 deg C), showing that the high fill factor provides good heat transfer out of the slot even with large slot widths in the case of the 6 slot cSynRM. The temperature is well within the specification of Class F insulation systems.

VI. Conclusion

The paper has presented for the first time a 6 slot 4 pole synchronous reluctance motor with non-overlapping fractional-slot concentrated windings (cSynRM). The designed machine is robust, relatively low cost and is easier to manufacture than a conventional synchronous reluctance machine. The machine exhibits a high torque density, high efficiency with high overload capability. The machine overcomes the previously reported high torque ripple by good electromagnetic design of the rotor, this is still an area for continued research. The *d-q* axis inductances are found to vary spatially with rotor angle, defying fundamental assumptions of the *d-q* transformation. Torque quality in the machine is found

to be impacted by parasitic rotor saliencies and asynchronous airgap fields. The electromagnetic finite element model is verified by experimental results. The empirical data matches the FE predicted static torque waveforms, the *d-q* axis flux linkage magnetization curves and the *d-q* axis inductances with a high degree of accuracy. Subsequent calculations of the power factor and torque capability based on experimental data and calculation of the motors saliency ratio and torque index show that *d-q* analysis can still accurately predict machine performance even with the existence of a high level of airgap space harmonics due to the non-sinusoidal windings in the steady state, however its accuracy in dynamic transient simulations and sensorless control are then brought into question. Thermal measurements also show promising results in relation to the thermal rating of the machine.

ACKNOWLEDGMENT

This work was financially supported in part by Cummins Generator Technologies, Stamford, UK.

APPENDIX

Coil End-winding Leakage Inductance Calculation

The lumped end winding leakage inductance for single coil of a three phase machine can be approximated for a stator number of slots Q_s, number of coil turns, N_{coil} in coil area, A, and coil pitch, τ_p [25];

$$L_{\text{ew(coil)}} = \frac{\mu_0 \tau_p (N_{\text{coil}})^2}{2} \ln\left(\frac{\sqrt{\pi}\tau_p}{\sqrt{2A}}\right) \qquad \text{(B1)}$$

The calculated lumped end winding inductance is 124.15μH, which is agreeable with the inductance calculation in Infolytica Motorsolve which uses a finite element method on a 3D end winding model to calculate this inductance and provides a value of 139.5 μH, as used in the MagNet model.

REFERENCES

[1] Moghaddam, R.; Gyllensten, F., "Novel High Performance SynRM Design Method, an Easy Approach for a Complicated Rotor Topology," *Industrial Electronics, IEEE Transactions on* , vol.PP, no.99, pp.1,1, 2014

[2] Moghaddam, R.R.; Magnussen, F.; Sadarangani, C., "Theoretical and Experimental Reevaluation of Synchronous Reluctance Machine," *Industrial Electronics, IEEE Transactions on* , vol.57, no.1, pp.6,13, Jan. 2010

[3] Bianchi, N.; Bolognani, S.; Bon, D.; Dai Pre, M., "Torque Harmonic Compensation in a Synchronous Reluctance Motor," *Energy Conversion, IEEE Transactions on* , vol.23, no.2, pp.466,473, June 2008

[4] Staton, D.A.; Miller, T. J E; Wood, S.E., "Maximising the saliency ratio of the synchronous reluctance motor," *Electric Power Applications, IEE Proceedings B* , vol.140, no.4, pp.249,259, Jul 1993

[5] Villet, W.T.; Kamper, M.J., "Variable-Gear EV Reluctance Synchronous Motor Drives—An Evaluation of Rotor Structures for Position-Sensorless Control," *Industrial Electronics, IEEE Transactions on* , vol.61, no.10, pp.5732,5740, Oct. 2014

[6] Moghaddam, R.-R.; Gyllensten, F., "Novel High-Performance SynRM Design Method: An Easy Approach for A Complicated Rotor Topology," *Industrial Electronics, IEEE Transactions on* , vol.61, no.9, pp.5058,5065, Sept. 2014

[7] Micallef, C.; Pickering, S.J.; Simmons, K.A.; Bradley, K.J., "Improved Cooling in the End Region of a Strip-Wound Totally Enclosed Fan-Cooled Induction Electric Machine," *Industrial Electronics, IEEE Transactions on* , vol.55, no.10, pp.3517,3524, Oct. 2008

[8] Staton, D.; Boglietti, A.; Cavagnino, A., "Solving the More Difficult Aspects of Electric Motor Thermal Analysis in Small and Medium Size Industrial Induction Motors," *Energy Conversion, IEEE Transactions on* , vol.20, no.3, pp.620,628, Sept. 2005

[9] Spargo, C.M.; Mecrow, B.C.; Widmer, J.D., "Application of fractional slot concentrated windings to synchronous reluctance machines," *Electric Machines & Drives Conference (IEMDC), 2013 IEEE International* , vol., no., pp.618,625, 12-15 May 2013

[10] Spargo. C, *et al*, "Higher Pole Number Synchronous Reluctance Machines with Fractional Slot Concentrated Windings," *Power Electronics, Machines and Drives (PEMD 2014), 7th IET International Conference on*, 8 – 10 April 2014

[11] Spargo, C.M.; Mecrow, B.C.; Widmer, J.D., "A Seminumerical Finite-Element Postprocessing Torque Ripple Analysis Technique for Synchronous Electric Machines Utilizing the Air-Gap Maxwell Stress Tensor," *Magnetics, IEEE Transactions on* , vol.50, no.5, pp.1,9, May 2014

[12] Miller. T.J.E, 'Switched Reluctance Motors and Their Control', Magna Physics Press, 1991

[13] Abdel-Khalik, A.S.; Ahmed, S.; , "Performance Evaluation of a Five-Phase Modular Winding Induction Machine," Industrial Electronics, IEEE Transactions on , vol.59, no.6, pp.2654-2669, June 2012

[14] EL-Refaie, A.M., "Fractional-Slot Concentrated-Windings Synchronous Permanent Magnet Machines: Opportunities and Challenges," *Industrial Electronics, IEEE Transactions on* , vol.57, no.1, pp.107,121, Jan. 2010

[15] Widmer, J.D.; Spargo, C.M.; Atkinson, G.J.; Mecrow, B.C., "Solar Plane Propulsion Motors With Precompressed Aluminum Stator Windings," *Energy Conversion, IEEE Transactions on*, vol.PP, no.99, pp.1-8, 2014

[16] Emetor Winding Calculator; http://www.emetor.com, 02/06/2014, 9:25am

[17] Cros, J.; Viarouge, P., "Synthesis of high performance PM motors with concentrated windings," *Energy Conversion, IEEE Transactions on* , vol.17, no.2, pp.248,253, Jun 2002

[18] Magnussen, F.; Sadarangani, C.; , "Winding factors and Joule losses of permanent magnet machines with concentrated windings," Electric Machines and Drives Conference, 2003. IEMDC'03. IEEE International , vol.1, no., pp. 333- 339 vol.1, 1-4 June 2003

[19] Staton, D.A.; Miller, T. J E; Wood, S.E., "Maximising the saliency ratio of the synchronous reluctance motor," *Electric Power Applications, IEE Proceedings B* , vol.140, no.4, pp.249,259, Jul 1993

[20] Miller, T. J E; Hutton, A.; Cossar, C.; Staton, D.A., "Design of a synchronous reluctance motor drive," *Industry Applications, IEEE Transactions on* , vol.27, no.4, pp.741,749, Jul/Aug 1991

[21] I. Boldea, Reluctance Synchronous Machines and Drives, Oxford University Press (August 1, 1996)

[22] Morales-Caporal, R.; Pacas, M., "Encoderless Predictive Direct Torque Control for Synchronous Reluctance Machines at Very Low and Zero Speed," *Industrial Electronics, IEEE Transactions on* , vol.55, no.12, pp.4408,4416, Dec. 2008

[23] E. Schmidt, M. Sušić, 'Finite element analysis of permanent magnet synchronous machines with fractional slot tooth coil windings', e & i Elektrotechnik und Informationstechnik, March 2011, Volume 128, Issue 3, pp 86-94

[24] Dai, N. Q.; Dutta, R.; Rahman, M. F., "Comparative performance analysis of field-oriented control and direct torque control for a fractional-slot concentrated winding interior permanent magnet synchronous machine," *Electrical Machines (ICEM), 2012 XXth International Conference on* , vol., no., pp.879,885, 2-5 Sept. 2012

[25] D. Hanselman, 'Brushless permanent-magnet motor design', McGraw-Hill, 1994